



**HAL**  
open science

# Modeled subglacial water flow routing supports localized intrusive heating as a possible cause of basal melting of Mars' south polar ice cap

Neil S Arnold, Susan J. Conway, F. E G Butcher, M. R Balme

## ► To cite this version:

Neil S Arnold, Susan J. Conway, F. E G Butcher, M. R Balme. Modeled subglacial water flow routing supports localized intrusive heating as a possible cause of basal melting of Mars' south polar ice cap. *Journal of Geophysical Research. Planets*, 2019, 124 (8), pp.2101-2116. 10.1029/2019JE006061 . hal-02268375

**HAL Id: hal-02268375**

**<https://hal.science/hal-02268375>**

Submitted on 20 Aug 2019

**HAL** is a multi-disciplinary open access archive for the deposit and dissemination of scientific research documents, whether they are published or not. The documents may come from teaching and research institutions in France or abroad, or from public or private research centers.

L'archive ouverte pluridisciplinaire **HAL**, est destinée au dépôt et à la diffusion de documents scientifiques de niveau recherche, publiés ou non, émanant des établissements d'enseignement et de recherche français ou étrangers, des laboratoires publics ou privés.

1 Modeled subglacial water flow routing supports localized intrusive heating as a possible  
2 cause of basal melting of Mars' south polar ice cap

3

4 **N. S. Arnold<sup>1</sup>, S. J. Conway<sup>2</sup>, F. E. G. Butcher<sup>3</sup> and M. R. Balme<sup>3</sup>**

5 <sup>1</sup>A Scott Polar Research Institute, University of Cambridge, Lensfield Road, Cambridge CB2  
6 1ER, UK.

7 <sup>2</sup>CNRS, Laboratoire de Planétologie et Géodynamique, UMR 6112, 2, rue de la Houssinière BP  
8 92208, France.

9 <sup>3</sup>School of Physical Sciences, The Open University, Walton Hall, Milton Keynes MK7 6AA,  
10 UK.

11 Corresponding author: Neil Arnold ([nsa12@cam.ac.uk](mailto:nsa12@cam.ac.uk))

12 **Key Points:**

- 13 • We calculate the subglacial hydraulic potential for the Martian south polar ice cap from  
14 measured surface topography and ice thickness.
- 15 • The recently-observed area of inferred basal melt does not occupy a predicted depression  
16 in the subglacial hydraulic potential surface.
- 17 • We argue this supports the hypothesis that local geothermal heating could be responsible  
18 for this area of liquid.  
19

20 **Abstract**

21 The discovery of a ~20 km wide area of bright subsurface radar reflections, interpreted as liquid  
22 water, beneath the Martian south polar layered deposits (SPLD) in data from the Mars Advanced  
23 Radar for Subsurface and Ionosphere Sounding (MARSIS) instrument, and the discovery of two  
24 geologically recent potential eskers (landforms produced by subglacial melt) associated with  
25 viscous flow features in Martian mid-latitudes, has suggested recent basal melting of Martian ice  
26 deposits may be feasible, possibly due to locally elevated geothermal heating. Locations of  
27 terrestrial subglacial lakes and major drainage axes have been successfully predicted from  
28 subglacial hydraulic potential surfaces calculated from surface topography and ice thickness.  
29 Here, we use surface topography from the Mars Orbiter Laser Altimeter and SPLD bed  
30 elevations derived from MARSIS data to calculate the subglacial hydraulic potential surface  
31 beneath the SPLD and determine whether the observed high reflectance area coincides with  
32 predicted subglacial lake locations. Given the sensitivity of terrestrial predictions of lake  
33 locations to basal topography, we derive over 1000 perturbed topographies (using noise statistics  
34 from the MARSIS data) to infer the most likely locations of possible subglacial water bodies and  
35 drainage axes. Our results show that the high reflectance area does not coincide with any  
36 substantial predicted lake locations; three nearby lake locations are robustly predicted however.  
37 We interpret this result as suggesting that the high reflectance area (assuming the interpretation  
38 as liquid is correct) is most likely a hydraulically-isolated patch of liquid confined by the  
39 surrounding cold-based ice, rather than a topographically-constrained subglacial lake.

40

41 **Plain Language Summary**

42 Mars' present-day ice deposits are generally assumed to be frozen throughout given its cold  
43 climate. However, new evidence from orbital radar data suggests a possible present-day ~20 km  
44 wide area of liquid water beneath Mars' south polar ice cap. Recently-discovered landforms in  
45 Mars' mid-latitudes have been interpreted as eskers (landforms produced by flowing meltwater  
46 beneath glaciers on Earth) and also suggest that subglacial melt may be feasible in Mars' recent  
47 past. Subglacial lakes are common on Earth, and their locations have been successfully predicted  
48 from ice surface topography and ice thickness, in conjunction with theories for subglacial water  
49 flow. In this paper we use the surface topography and ice thickness data for Mars' south polar ice  
50 cap to calculate the theoretical locations of possible subglacial lakes, and compare these with the  
51 location of the possible present-day area of liquid water. The observed patch of possible liquid  
52 water does not coincide with the lake locations we predict. We interpret this result as implying  
53 that the liquid water is most likely to be an isolated patch of liquid, possibly caused by locally-  
54 raised geothermal heating, and which is fixed in position by the surrounding frozen ice, rather  
55 than the liquid forming a topographically-constrained subglacial lake.

## 56 1 Introduction

57 Ice sheets, glaciers and ground ice distributed between Mars' poles and mid-latitudes  
58 [e.g. *Plaut et al.*, 2007; *Levy et al.*, 2014; *Souness and Hubbard*, 2012; *Head et al.*, 2003] contain  
59 a total volume of water ice (estimated as  $\sim 3.5 \times 10^6 \text{ km}^3$ ), comparable to that of all glaciers on  
60 Earth excluding the East Antarctic Ice Sheet [*Levy et al.*, 2014], Mars' existing ice deposits are  
61 thought to have formed  $\sim 100$ s to Myrs ago [e.g. *Head et al.*, 2003; *Arfstrom and Hartmann*,  
62 2005; *Butcher et al.*, 2017; *Conway et al.*, 2018], with landforms and models also indicating  
63 episodic glaciation of different regions of Mars' surface over billions of years [e.g. *Fastook et*  
64 *al.*, 2008; *Wordsworth et al.*, 2013; *Butcher et al.*, 2016]. Glaciers and ice sheets insulate a  
65 planet's surface, trapping geothermal heat from the planetary interior and frictional heat  
66 produced by ice flow, typically making their beds warmer than their surfaces. However, it is  
67 commonly thought that Mars' climate has been cold and dry for  $\sim 2\text{--}3$  Gyr, and hence that the  
68 existing glaciers and ice caps have most probably been frozen throughout [e.g. *Levy et al.*, 2016],  
69 although there is some evidence for spatially-limited, ephemeral supraglacial melt [e.g. *Fassett et*  
70 *al.*, 2010]. The migration of ice between different reservoirs at different locations on Mars over  
71 this period is thought to have taken place via sublimation and (solid) precipitation, rather than  
72 melt [*Bramson et al.* 2017].

73 In contrast, recent geomorphological studies found evidence for localized melting  
74 beneath two existing mid-latitude glaciers around 110–150 Myr ago (Ma), in the form of  
75 subglacially-deposited eskers in Phlegra Montes and Tempe Terra [*Gallagher and Balme*, 2015,  
76 *Butcher et al.*, 2017]. Furthermore, that present day glaciers and ice caps are frozen throughout  
77 has also been challenged by the discovery of possible present-day liquid water beneath Mars'  
78 South Polar Layered Deposits [SPLD; *Orosei et al.*, 2018], based on anomalously bright  
79 subsurface reflections recorded by the MARSIS (Mars Advanced Radar for Subsurface and  
80 Ionospheric Sounding) instrument in a well-defined, 20 kilometer wide zone centered at 193°E,  
81 81°S. In all three locations, elevated geothermal heating (e.g. due to localized magmatic  
82 intrusions) has been proposed as a possible source of the heat needed to melt the basal ice under  
83 cold current and recent Martian climate conditions [*Sori and Bramson*, 2019, *Butcher et al.*,  
84 2017, *Gallagher and Balme*, 2015]. In addition, perchlorate salts, which substantially lower the  
85 melting point of ice to around  $\sim 200$  to 230K depending on the concentration and species of  
86 perchlorate, may be highly enriched in the basal layers of the Martian polar ice caps [*Fisher et*  
87 *al.*, 2010; *Sori and Bramson*, 2019].

88 Subglacial water is far more common on Earth, occurring beneath the bulk of terrestrial  
89 valley glaciers, and both the Greenland and Antarctic Ice Sheets. In the case of Antarctica, large  
90 numbers of subglacial lakes, including Lake Vostok, the 6<sup>th</sup> largest (by volume) lake on Earth,  
91 have been detected by observing bright reflectances from numerous ground penetrating radar  
92 systems. Movement of water between subglacial lakes in large episodic drainage events has also  
93 been observed using localized changes in surface topography as lakes drain and fill. There is also  
94 a great deal of evidence for widespread subglacial meltwater in the landscapes occupied by ice  
95 during the Quaternary (and earlier) glaciations on Earth [e.g. *Shreve*, 1985; *Storrar et al.*, 2013,  
96 *Stroeven et al.*, 2016; *Clark et al.*, 2017].

97 The physics of subglacial water flow are well known. *Flowers* [2015] provides a  
98 comprehensive review, but briefly, the overall pattern of subglacial water flow is governed by  
99 the subglacial potential surface (calculated from the subglacial topography and ice thickness  
100 distribution; *Shreve*, [1972]). Local depressions in the potential surface form the nuclei for

101 possible subglacial lakes, as water cannot escape from such depressions until it fills to the  
102 elevation of the local ‘spill point’, the elevation of the lowest point in the constraining potential  
103 surface. Calculations of subglacial potential using digital elevation models (DEMs) of ice  
104 surfaces and ice thickness (or bed elevations) have proved very successful at predicting  
105 subglacial lake locations and volumes for terrestrial ice sheets. In a study of Antarctic lake  
106 locations, *Willis et al.*, [2016] show that the centers of lake locations predicted using the  
107 calculated subglacial potential surface were a mean distance of 6.3 km from the centers of the  
108 379 known (in 2016) lakes. *Willis et al.*, [2016] predict around 100 times as many possible lake  
109 locations as the number of known lakes however. Some of this mis-match will be due to the size  
110 and remoteness of Antarctica, meaning that the current lake inventory will be incomplete.  
111 However, some of the mis-match will be due to errors of commission, where the potential  
112 surface predicts a lake where no lake exists. Such errors may be caused by inaccuracies in the  
113 surface or bed DEMs due to inaccuracies and/or resolution effects in the sensors, or the  
114 interpolation of relatively sparse point data onto a regular grid.

115         Several studies have shown that quite small changes in the bed and particularly the  
116 surface elevation can cause substantial changes in predicted subglacial water flow directions and  
117 lake locations. *Wright et al.*, [2008] found that raising three grid cells in the surface DEM by  
118 10 m led to water flow switching between two major outlets from East Antarctica, and  
119 subsequently lowering another four surface DEM cells by 10 m led to another switch between  
120 two other large outlet glaciers. *Le Brocq et al.*, [2009] report similar sensitivity to small (~10 m)  
121 changes in surface elevation that divert flow between two major ice streams draining the Siple  
122 Coast of West Antarctica.

123         Uncertainties in data will also affect the predicted location of subglacial lakes.  
124 *Livingstone et al.*, [2013a] used current bed topography and modeled ice thickness distributions  
125 and isostatic effects from a suite of ice-dynamic reconstructions of the geometry of the North  
126 American Ice Sheets during the last glaciation on Earth to predict possible subglacial palaeo-lake  
127 locations. They found that lake locations (and inferred water flow directions) were highly  
128 sensitive to the configuration of the ice sheet at particular stages during ice sheet growth and  
129 decay, and depended in some instances on the choice of model and the predicted ice thickness  
130 distribution. They found that some predicted lakes were persistent through time, and were also  
131 predicted by many of the modeled ice sheet configurations, whereas other predicted lakes were  
132 present in fewer simulations, or were more transient features through time. Overall, deeper  
133 predicted lakes in areas of more pronounced topography (e.g. beneath the Cordilleran Ice Sheet  
134 in western North America) were more persistent. In another study, *Livingstone et al.*, [2013b]  
135 investigated the impact of errors or uncertainty in the basal topography of Antarctica on  
136 predicted subglacial lake locations by perturbing the bed topography using random noise with a  
137 standard deviation equal to the uncertainty in the bed elevation. They performed 50 such  
138 perturbations to produce a ‘persistence map’ of lakes, in which the most persistent lakes were  
139 those which were predicted in the majority of the perturbed-bed experiments.

140         In this paper we use gridded surface and ice thickness maps for the Martian South Polar  
141 Layered Deposit [SPLD; *Plaut et al.*, 2007] to calculate the subglacial hydraulic potential. From  
142 this, we infer the locations of depressions in the potential surface that would be expected to  
143 confine possible subglacial water bodies were basal meltwater available beneath the SPLD. We  
144 also predict the main drainage axes that any possible flowing water would be expected to follow.  
145 In order to address uncertainties in the bed elevation data (due to the limited resolution of the ice

146 thickness data from the MARSIS sensor, in particular) we adopt a similar approach to  
 147 *Livingstone et al.*, [2013b] and perform a suite of lake location calculations using DEMs derived  
 148 from the raw MARSIS data, the mean and median of all radar footprints crossing each point (cf.  
 149 *Orosei et al.*, [2018]), and a set of 1000 DEMs interpolated from randomly perturbed bed  
 150 elevation data, with perturbations calculated using the statistical properties of the elevation  
 151 differences within the MARSIS data. We use different assumptions of the density of the inferred  
 152 subglacial liquid, from pure water to saturated perchlorate brine, and we also investigate the  
 153 impact of the spatial resolution of the interpolated DEMs. From this set of calculations we  
 154 determine the most persistent predicted lake locations and predicted water flow paths. We then  
 155 consider the implications of these predictions by comparing the predicted lake locations and  
 156 persistence values with the high reflectance area (HRA) reported by *Orosei et al.*, [2018]. We  
 157 use these predictions to consider the likelihood (or otherwise) of a well-connected subglacial  
 158 drainage system beneath the Martian SPLD, or whether the possible water body inferred from  
 159 radar reflectance [*Orosei et al.*, 2018] is more likely to be a hydraulically-isolated feature.

## 160 2 Methods

### 161 2.1 Modeling lake locations

162 We calculate subglacial hydraulic potential ( $\phi$ ) from the bed and surface elevation  
 163 [*Shreve*, 1972]:

$$164 \quad \phi = \rho_w g Z + k \rho_i g H \quad [1]$$

165 where  $g$  is gravity ( $3.711 \text{ m s}^{-2}$ );  $\rho_w$  is the density of the subglacial liquid, ranging from  
 166  $1000 \text{ kg m}^{-3}$  for pure water to  $1980 \text{ kg m}^{-3}$  for saturated perchlorate brine [*Fisher et al.*, 2010];  $Z$   
 167 is the bed elevation (m),  $\rho_i$  is the ice density (here taken to be  $910 \text{ kg m}^{-3}$ , given the uncertainty  
 168 concerning the overall density of the Martian SPLD; [e.g. *Zuber et al.*, 2007; *Plaut et al.*, 2007;  
 169 *Wieczorek*, 2008]) and  $H$  is the ice thickness (m).  $k$  is a dimensionless factor which represents the  
 170 influence of ice overburden pressure on the local subglacial water pressure, with  $k = 1$  implying  
 171 the water pressure is at the ice overburden pressure, and  $k = 0$  implying the subglacial water is at  
 172 atmospheric pressure. In terrestrial systems,  $k$  is variable in time and space, especially in  
 173 situations closer to the ice margin where the ice is thinner and/or heavily affected by seasonal  
 174 meltwater. In the interiors of ice sheets, where the ice is thicker, and especially for Antarctica,  
 175 measured water pressures are typically very close to ice overburden. Given the location of the  
 176 HRA in the interior of the SPLD, and the  $\sim 1500 \text{ m}$  inferred ice thickness, we assume  $k = 1$  in our  
 177 simulations.

178 Equation 1 can usefully be re-cast into an alternative formulation which uses  $Z$  as before,  
 179 and also the ice surface elevation,  $S$ , where  $S = Z + H$ :

$$180 \quad \phi = (\rho_w - k \rho_i) g Z + k \rho_i g S \quad [2]$$

181 This alternative formulation highlights the typical dominance (for high  $k$  values) of the  
 182 ice surface elevation on the subglacial hydraulic potential due to the small difference in the  
 183 density of ice and water. For the SPLD, however, if the liquid layer is a high solute-  
 184 concentration brine,  $\rho_w$  will be higher, increasing the importance of the basal topography in

185 determining the subglacial hydraulic potential. Given this, we use  $\rho_w = 1980 \text{ kg m}^{-3}$  in the bulk  
186 of our calculations, but we also perform a set of runs in which  $\rho_w$  is varied in 11 equal steps  
187 between 1000 and 1980  $\text{kg m}^{-3}$ . Uncertainty in the ice density [e.g. *Zuber et al.*, 2007; *Plaut et*  
188 *al.*, 2007; *Wieczorek*, 2008] will have an opposing effect. A higher ice density will increase the  
189 dominance of the ice surface elevation, reducing the role played by basal topography on the  
190 subglacial potential, and reducing the impact of possible higher liquid density. If the ice density  
191 exceeds the liquid density, this will reverse the sign of the first term in Eq. 2 (although this  
192 negative value will be compensated to some extent by the increased value of the second term,  
193 depending on the relative values of the ice and liquid densities, and the surface and bed  
194 elevations). To assess the likely maximum impact of this effect, we also perform a run using an  
195 ice density of 1200  $\text{kg m}^{-3}$  [*Zuber et al.*, 2007; *Wieczorek*, 2008] and a liquid density of 1000  $\text{kg}$   
196  $\text{m}^{-3}$ .

197 We calculate lake locations using the flow accumulation algorithm developed by *Arnold*  
198 [2010], as applied by *Willis et al.*, [2016] for Antarctica, using gridded  $\phi$  values calculated from  
199 the surface topography, inferred bed topography, and  $\rho_w$  value for each experiment. The  
200 calculated hydraulic potential (hereafter shortened to potential) gradient allows inferred water  
201 flow directions to be calculated for each DEM cell; the algorithm assigns each DEM cell an area,  
202 based on its own area plus the total area upstream of the cell for which water flow-lines pass  
203 through the cell. The algorithm also identifies all cells in the potential surface that are at a lower  
204 potential than all their neighbours (and which therefore act as ‘dead end’ in the flow  
205 accumulation algorithm) and defines them as ‘sink’ cells. Together, the water flow directions and  
206 sink cells allow local subglacial catchments (a group of contiguous cells which all drain toward  
207 the sink) to be determined. Sink cells also form the nucleus for possible subglacial lakes; the  
208 algorithm ‘floods’ each sink cell to find the elevation of the lowest cell in the catchment  
209 surrounding the sink cell over which water would spill into a lower potential downstream cell  
210 (and hence, into an adjacent catchment). This spill point cell defines the maximum depth  
211 (relative to the elevation of the sink cell), area, and volume of each predicted possible lake, and  
212 also allows the routing algorithm to pass the total catchment area from catchment to catchment  
213 downstream until the model reaches the edge of the ice cap. In this way, the algorithm builds up  
214 the topology of possible subglacial water flow, linking the individual catchments and lakes  
215 together into arborescent structures analogous to typical stream networks. Major drainage axes  
216 appear as distinct ‘threads’ across the potential surface with large upstream area values, meaning  
217 a large number of upstream cells ultimately feed their area through such cells. Upstream source  
218 areas, or more isolated areas, show much lower upstream area values. Cells within a lake are  
219 assigned an area equal to the total upstream area above the spill point for that lake. Lakes on the  
220 main drainage axes appear therefore as ‘beads’ of high upstream area, but even lakes in upstream  
221 or more isolated areas are easily identified as areas of uniform, locally-high upstream area  
222 values.

## 223 2.2 Ice surface and bed topography

224 For the ice surface elevation, we use the south polar MOLA gridded topographic map for  
225 Mars at 128 pixels per degree (460 m per pixel) resolution (Figure 1a; *Smith et al.*, [2001]) in all  
226 experiments. For the bed topography, we use the MARSIS sub-spacecraft latitude and longitude,  
227 and the inferred elevation of the basal reflector (used to produce the ice thickness and hence bed  
228 elevation datasets from *Plaut et al.*, [2007]), supplemented with the additional data reported in

229 *Orosei et al.*, [2018], to provide the x,y,z point-cloud data needed for interpolation of the bed  
230 DEMs. We perform our experiments for the  $200 \times 200$  km area centered around  $193^\circ\text{E}$ ,  $81^\circ\text{S}$  that  
231 contains the high-reflectance signal reported by *Orosei et al.*, [2018]; Figure 1b. In order to  
232 facilitate direct comparison with the results reported in *Orosei et al.* 2018, we also adopt a north-  
233 down orientation in Figure 1b and subsequent figures. 86 points from *Plaut et al.* [2007] fall in  
234 our study area, and allow interpolation outside the area covered by the point cloud data presented  
235 in *Orosei et al.* [2018]. In order to compare our results directly with those from *Orosei et al.*,  
236 [2018], we perform the bulk of our experiments at the 200 m resolution used by *Orosei et al.*,  
237 [2018], but we also derive DEMs at 500 m, 1000 m, 2500 m and 5000 m resolution to test the  
238 impact of DEM resolution. Following *Plaut et al.*, [2007], we use natural neighbour  
239 interpolation, and apply noise to the MARSIS data from *Orosei et al.* [2018] as detailed below  
240 for our perturbation analysis. We pin the edge of the study area to the elevation taken from the  
241 overall SPLD gridded bed elevation map [*Plaut et al.*, 2007].

242 The vertical resolution of the MARSIS sensor is around 100–150 m [e.g. *Plaut et al.*,  
243 2007], controlled ultimately by the frequency and time resolution of the sensor. Inferring bed  
244 elevation from the radar returns also requires knowledge of the dielectric constant of the  
245 material; we use the values (and hence elevations) reported by *Orosei et al.* [2018]. The noise we  
246 apply to the data (detailed below) effectively allows us to simulate the impact of uncertainty in  
247 the dielectric constant however. The Fresnel radius (ground footprint) is  $\sim 3\text{--}5$  km [*Orosei et al.*,  
248 2018] and varies along-track and across-track. 76,800 individual data points are available within  
249 the study area, from 27 individual satellite tracks (Figure 2a). As can be seen in Figure 2a,  
250 however, the inferred SPLD thickness along the tracks varies considerably over quite short  
251 distances (well within the sensor footprint), which suggests that possible local variations in the  
252 dielectric, sensor resolution effects, or other noise sources strongly affect the inferred elevation.  
253 The along-track spacing of the points varies from  $\sim 30$  to  $\sim 90$  m, meaning that there is  
254 considerable footprint overlap along the tracks, and several sets of tracks are also close together,  
255 running nearly parallel to each other, or cross. This overlap between the footprints of the  
256 individual measurement points gives us information on the local variability or uncertainty in the  
257 inferred SPLD thickness in the MARSIS data. In order to estimate the statistical properties of  
258 this uncertainty, and provide a measure of the noise within the data, we identify all the points  
259 within the Fresnel radius of the sensor for each point, and use these to calculate the mean (Figure  
260 2b) and median (Figure 2c) height differences, and the standard deviation (Figure 2d) of the  
261 height differences, between each original point and the other points within the Fresnel radius.

262 Figure 3a shows the overall distribution of in-radius elevation differences, with the  
263 calculated mean and standard deviation of height difference. It approximates a normal  
264 distribution, though with a more marked central peak. However, some individual points deviate  
265 quite markedly from their neighbours; Figure 3b-d shows the distribution for the points with the  
266 maximum (Figure 3b) and minimum (Figure 3c) mean in-radius elevation difference, and the  
267 point with the largest standard deviation (Figure 3d) of in-radius elevation difference. Of the  
268 76,800 points, 64,496 have a standard deviation of the in-radius elevation difference smaller than  
269  $\pm 1$  standard deviation for the total set. The number of in-radius points varies between 108 and  
270 2362, with a mean value of 665 in-radius points per point.

271 We create a set of bed DEMs (shown in Figure 4 at 200 m resolution) for the hydraulic  
272 potential and flow routing calculations using the raw MARSIS points from *Orosei et al.*, [2018],



273 (Figure 4a); and the mean (Figure 4b), median (Figure 4c), minimum, and maximum of the  
274 elevation differences within the Fresnel radius as above. The minimum and maximum  
275 topographies were judged to be implausible due to the very large height differences produced in  
276 some areas, and are not used further. We then use a form of Monte-Carlo analysis to create a set  
277 of 1000 perturbed bed topographies by applying a random elevation change to each data point  
278 drawn from a normal distribution with the calculated mean and standard deviation of the in-  
279 radius elevation differences for that point. We apply the flow accumulation algorithm to each  
280 perturbed DEM, which then allows us to calculate a probability value that any given pixel is  
281 within a lake for the set of 1000 model runs. We also create a DEM (dubbed the mean-perturbed  
282 DEM) using the mean elevation of each cell calculated from the set of individual perturbed  
283 topographies (Figure 4d). We also apply the flow accumulation algorithm to the same set of  
284 DEMs at reduced resolution, but focus mainly on the 200 m resolution results for direct  
285 comparison with *Orosei et al.*, [2018].

286 Figure 4 shows that the mean, median and mean-perturbed 200 m resolution topographies  
287 are considerably smoother than that produced by the raw data. For all four, however, the impact  
288 of some of the individual satellite tracks can still be seen, such as the straight, deep trough  
289 running NNW from the S (top) edge of the area. This effect is reduced most in the mean-  
290 perturbed topography, which we therefore use in the series of experiments to investigate the  
291 possible impact of variable  $\rho_w$  values.

### 292 **3 Results**

293 Figure 5 shows the common logarithm of the flow accumulation results for the four 200  
294 m resolution topographies shown in Figure 4, using  $\rho_w$  of  $1980 \text{ kg m}^{-3}$ .

295 Possible lake locations are seen as the broad patches with high, uniform flow  
296 accumulation values (yellows in Figure 5). The overall drainage trend across the majority of the  
297 area is towards the east-north-east (left/bottom left) in all four simulations, driven by the effect of  
298 the overall slope of the SPLD surface topography in the area (Figure 1b) on the subglacial  
299 hydraulic potential (Eq. 2). The effect of the surface scarps in the north-west (bottom right) of  
300 the area (Figure 1b) can also be clearly seen as the thinner ice downstream of the scarps leads to  
301 local low subglacial potential values which act as large possible lake locations. Away from the  
302 scarps, however, where the SPLD surface topography is much flatter, the basal topography acts  
303 as the major control on predicted possible lake locations. Depressions in the bed form the foci for  
304 numerous possible lakes, especially in the rougher raw topography DEM (Figure 5a). However,  
305 what is clear is that the area of high basal reflectance does not coincide with a substantial  
306 predicted possible lake location in any reconstruction.

307 Figure 6 shows the  $2500 \text{ km}^2$  central area around the HRA in more detail. Consistently,  
308 three substantial possible lake locations are predicted nearly adjacent to the HRA; an irregularly  
309 shaped lake to the south-west (upper right) of the HRA; a rounder lake to the east (left), and a  
310 lake with a more variable extent to the south-east (upper left). For the raw topography DEM,  
311 several smaller lake locations are predicted within the HRA. These have lower flow  
312 accumulation values than the three larger adjacent lakes, however, and are topologically more  
313 isolated. In topological terms, the SW lake is linked to the E lake via a drainage axis running  
314 through the HRA from W to E in the mean and mean perturbed topographies (Figures 6b and d).

315 For the raw topography DEM (Figure 6a), the SW lake flows into the SE lake, and then to the E  
316 lake, with the predicted drainage axis touching the southern tip of the HRA. For the median  
317 topography DEM (Figure 6c), the routing is different again. The SW lake extends beyond the  
318 southern (top) edge of the study area, and flow is directed into the southern edge of the SE lake  
319 (outside the area shown in the figure), and then to the E lake; no substantial drainage axis crosses  
320 the HRA.

321 Figure 7a shows the probability values (P) for whether any given pixel is part of a  
322 possible lake from the set of 1000 perturbed topography runs. P is calculated by dividing the  
323 number of runs in which a pixel is calculated to be within a lake by the total number of runs.  
324 Thus,  $P = 0$  for a pixel which was never calculated to be in a lake and  $P = 1$  for a pixel which  
325 was calculated to be in a lake in all simulations. Here, the overall position of the three large  
326 adjacent predicted possible lakes is robust to perturbation using the calculated elevation variation  
327 statistics, although their exact extents vary (with the edges of the lakes having lower pixel  
328 probabilities), particularly for the southern extent of the SW lake. A small but persistent lake also  
329 appears in the southern part of the HRA that is less apparent in the single topography  
330 calculations (Figures 5 and 6). The individual satellite tracks are visible, as small predicted  
331 possible lakes will form in some topographies when an individual point is randomly moved  
332 downwards by a large amount, producing a deep, small depression, or when nearby points are  
333 moved upwards producing a depression between them. Figure 7b shows the mean flow  
334 accumulation values for the 1000 perturbed-topography runs. This again shows the persistence of  
335 the main predicted possible lakes; the lake edges are less sharp than for the single-topography  
336 runs, as pixels nearer the margins which are only calculated to be in lakes in some perturbed  
337 topographies will have lower mean flow accumulation values. There is also some blurring of the  
338 main drainage axes as calculated routing between the lakes will vary between the different  
339 perturbed topographies, but again, a drainage axis running W-E across the southern part of the  
340 HRA is visible, as occurs in the mean and mean-perturbed topographies (Figures 5 and 6b and  
341 d).

342 Figures 7c–f show the results for the variable liquid and ice density experiments. Figure  
343 7c shows the probability that any given pixel is part of a lake and Figure 7d shows the mean flow  
344 accumulation values for the 11 variable liquid density runs. Figure 7e shows the results for the  $r_w = 1000 \text{ kg m}^{-3}$  run, and Figure 7f the results for the  $r_i = 1200 \text{ kg m}^{-3}$  and  $r_w = 1000 \text{ kg m}^{-3}$  run. As  
345 implied by Eq. 2, for lower-density liquid the impact of bed topography is heavily reduced, and  
346 the surface slope dominates. For  $r_w = 1000 \text{ kg m}^{-3}$ , calculated lake occurrence in the vicinity of  
347 the HRA is virtually eliminated (Figure 7e). As liquid density increases, the SE lake begins to  
348 form at the lowest liquid density, and increases in extent most rapidly, as shown by the largest  
349 area of high probability (Figure 7c) and the largest area of high (bright yellow) mean flow  
350 accumulation values (Figure 7d). The SW and E lakes only become more extensive for inferred  
351 density  $> \sim 1600 \text{ kg m}^{-3}$ , with smaller areas of high probability (Figure 7c) and high mean flow  
352 accumulation values (Figure 7d). The drainage axis from the SW to E lake through the HRA is  
353 present in all variable-density runs (Figure 7d). For the run with  $r_i = 1200 \text{ kg m}^{-3}$  and  $r_w = 1000$   
354  $\text{kg m}^{-3}$  (Figure 7f), the overall pattern of flow is similar to the  $r_w = 1000 \text{ kg m}^{-3}$  run (Figure 7e)  
355 particularly within the HRA, which shows no predicted lake occurrence. The small predicted  
356 lake upstream of the location of the SE lake is caused by the increased impact of the thicker ice  
357 over the deep bed depression in this area preventing water from being routed through the  
358 depression, forcing water to flow around the bed depression.  
359

360 Figure 8 shows the mean flow accumulation values from the set of 1000 reduced  
361 resolution perturbed-topography runs (the equivalent to the 200 m resolution results shown in  
362 Figure 7b). These clearly show that resolution does not affect the location of the predicted  
363 possible lakes, nor the route of the drainage axis from the SW to E lake through the HRA. Only  
364 at the coarsest resolution (5000 m, Figure 8d) does the pattern start to break down somewhat,  
365 with the SW and E lakes remaining as separate entities, but linked by a much broader drainage  
366 axis through the HRA.

#### 367 4 Discussion

368 Mapping the locations of depressions in subglacial hydraulic potential surfaces has  
369 proved very successful in terms of predicting the location of subglacial lakes and drainage axes  
370 on Earth. The robust results reported here, which show that the HRA beneath the SPLD does not  
371 occupy such a depression, but occurs within 10 to 20 km of three such possible depressions  
372 which do not show high radar reflectances [Orosei et al. 2018], therefore seems anomalous.  
373 However, there are critical differences between the vast majority of terrestrial subglacial lakes  
374 and a hypothesized lake (or area of basal liquid) beneath the SPLD. Almost all known subglacial  
375 lakes on Earth are fed by meltwater which flows into the lake basin from upstream, delivered by  
376 an active subglacial drainage system that covers the ice sheet bed, which is at the pressure  
377 melting point, over wide areas. For Antarctica, where large numbers of subglacial lakes are  
378 known to exist, the main water source is basal melt. Numerical modeling suggests mean  
379 subglacial melt rates around 2–5 mm yr<sup>-1</sup> beneath Antarctica, with some fast flowing areas  
380 reaching several hundred mm per year [e.g. Willis et al., 2016; Pattyn 2010, Llubes et al., 2006].  
381 Basal melt is generated by a combination of strain heating and geothermal heat flux; West  
382 Antarctica in particular exhibits some of the highest melt rates, as it is thought to have relatively  
383 high geothermal heat flux of over 120 mW m<sup>-2</sup> in places (versus a continent-wide average value  
384 of 30-60 mW m<sup>-2</sup>) [Martos et al., 2017], and contains areas of very fast-moving ice which  
385 generate large amounts of strain heating. These high basal melt rates lead to sometimes very  
386 substantial water fluxes [over 1 km<sup>3</sup> yr<sup>-1</sup>, Willis et al., 2016] into some active lakes near the  
387 margins of Antarctica, which can trigger cyclic drainage events which have been observed  
388 through their impact on the surface topography of the ice sheet [e.g. Wingham et al., 2006,  
389 Fricker et al., 2007]. Such conditions are therefore very different from those at the base of the  
390 SPLD.

391 As well as subglacial lakes with large catchments fed by near-ubiquitous basal melt (such  
392 as beneath Antarctica), subglacial lakes directly fed by localized high geothermal heat fluxes are  
393 known to exist on Earth. The most widely studied is Grimsvötn, a subglacial lake beneath  
394 Vatnajökull, a large ice cap in SW Iceland. This lake is known to fill due to subglacial melt  
395 driven by very high geothermal heating [estimated at 35–40 W m<sup>-2</sup>, Björnsson and  
396 Guðmundsson, 1993], and then drain catastrophically when the lake volume exceeds a threshold.  
397 Subglacial hydrological theory has proved rather successful at predicting the discharge  
398 hydrographs of these drainage events [e.g. Nye, 1976; Spring and Hutter, 1981, Fowler, 1999],  
399 and even (though with less certainty) the triggers of the drainage events [Fowler, 1999]. The key  
400 finding from Grimsvötn is that the lake forms in a topographic depression beneath the ice, which  
401 causes a low in the subglacial hydraulic potential. The lake surface, however, can reach a higher  
402 elevation than the top of the topographic lip of the basin as the subglacial potential increases in  
403 front of the lake due to thicker ice downstream. This reversed potential slope impounds the lake,

404 not the bed topography in itself. At some critical water level, however, the potential gradient  
405 reverses and the lake drains catastrophically, as the large water discharge enables rapid growth of  
406 an efficient subglacial drainage system. These drainage events result in catastrophic floods  
407 (jökulhlaups) beyond the ice cap margin, and result in the formation of pronounced cauldrons on  
408 the ice cap surface.

409 Figure 9 shows the surface and basal topography, and subglacial hydraulic potential, for a  
410 transect through the HRA located on the drainage axis between the SW and E depressions  
411 beneath the SPLD (shown in Figure 7b). The reverse gradient in subglacial potential that  
412 impounds the two predicted lakes can be clearly seen, but no such reverse gradient exists for the  
413 region occupied by the HRA.

414 In addition to local melt, Grimsvötn is thought to also receive melt from upstream [e.g.  
415 *Fowler, 1999*]; the ice cap is also at the pressure melting point, so once discharge from the lake  
416 is underway, no thermal barrier exists to prevent drainage. This also contrasts strongly with the  
417 situation beneath the SPLD. If locally-raised geothermal heating is necessary to raise the basal  
418 ice to the melting point [*Sori and Bramson, 2019*], the rate of filling of any putative lake would  
419 be far slower. This is because of the lower likely geothermal heating, more rapid loss of heat  
420 through the much colder ice within the SPLD, and the lack of any upstream catchment to feed  
421 additional melt into the hypothesized lake. The inferred liquid beneath the SPLD therefore seems  
422 to be trapped by a thermal ‘dam’, rather than by variations in the potential surface. This perhaps  
423 makes it less likely that the HRA is a true subglacial lake, in the sense of being constrained by  
424 topography.

425 The geophysical model results presented by *Sori and Bramson* [2019] show geothermal  
426 heating rising rapidly (over ~0.5 Myr) after the intrusion of a magma chamber beneath the HRA,  
427 and then falling more slowly (over the subsequent 1–2 Myr). If the HRA is indeed geothermally-  
428 heated liquid, it could therefore currently be on the ‘rising limb’ of heating, and getting larger; at  
429 its peak extent (though perhaps this is the least likely scenario due to the shorter duration of peak  
430 heating); or on the ‘falling limb’, and shrinking. If the former is the case, and the extent of basal  
431 melt increases in the future such that the area expands to encompass our predicted depressions in  
432 the potential surface, then we can speculate whether such an occurrence would allow a ‘true’  
433 subglacial lake, pinned by the topography, to form. We can also speculate if a rapid drainage  
434 event of this lake would occur if it reached some critical volume threshold. In the latter case, and  
435 especially if a drainage event had occurred in the past, it could be the case that some topographic  
436 signature on the surface of the SPLD might be manifest. Whilst Icelandic subglacial volcanism  
437 can produce cauldrons several hundred meters deep for ice typically up to ~500 m thick,  
438 numerical modeling [e.g. *Evatt and Fowler, 2007*] and observations [e.g. *Wingham et al., 2006,*  
439 *Fricker et al., 2007, 2009*] suggest changes in surface topography of a few metres for lakes of  
440 similar size to the HRA for the thicker ice, and pressure-driven drainage events, known to occur  
441 for Antarctic subglacial lakes. Such topographic signatures would be difficult to detect on the  
442 SPLD, but could perhaps be detected in derivatives of the highest resolution MOLA elevation  
443 data. Currently no such anomalous topography can be discerned on the ice surface over the  
444 HRA.

445 Our results do not suggest that the explanation of the HRA being caused by the presence  
446 of liquid water [*Orosei et al., 2018*] is any more or less likely due to it not being in a depression

447 within the calculated subglacial potential surface. Our results also suggest that spatially-limited  
448 geothermal heating seems unlikely to produce an active subglacial drainage system capable of  
449 sustaining flow across parts of the bed, but rather that spatially-limited heating may produce melt  
450 which is pinned *in-situ* by the surrounding frozen base. This suggests that more extensive basal  
451 melting, driven by a combination of a larger area of higher geothermal heating, thicker ice and  
452 warmer surface temperatures (all of which were more probable earlier in Mars' history, and in  
453 agreement with previous palaeo-environmental reconstructions [e.g. *Fastook et al.*, 2012;  
454 *Scanlon et al.*, 2018]), would be required for the occurrence of an active subglacial drainage  
455 system capable of moving large quantities of sediment, and therefore of forming the ancient  
456 [ $\sim$ 3.5–3.6 Ga; *Kress and Head* 2015; *Bernhardt et al.*, 2013] putative eskers in the south polar  
457 Dorsa Argentea Formation and Argyre Planitia [e.g., *Butcher et al.*, 2016; *Bernhardt et al.*,  
458 2013]. In the case of the younger (110–150 Ma) esker systems observed in Mars' mid-latitudes  
459 [*Gallagher and Balme*, 2015, *Butcher et al.*, 2017], however, widespread subglacial melt seems  
460 less likely given the colder Martian climate in the Amazonian. Mid-latitude glaciers are thought  
461 to have been more extensive during periods of high obliquity, however [e.g. *Baker and Head*  
462 2015], which would tend to warm the basal ice directly, and could lead to higher strain heating  
463 due to larger basal shear stress [*Butcher et al.*, 2017]. Coupled with locally elevated geothermal  
464 heat, this would make it more likely for the basal ice to reach the melting point in the area above  
465 the geothermal anomaly, especially if salts lowered the melting point of the basal ice. Were the  
466 melting to occur over a large enough area, this liquid might begin to flow down the potential  
467 surface or become impounded in depressions in the subglacial hydraulic potential surface as  
468 topographically-constrained subglacial lakes. The number and extent of such depressions in the  
469 potential surface would be increased if the basal liquid consisted of high-density brine. The  
470 possible growth of any such lakes during the onset-to-peak phase of heating could lead to them  
471 filling the depressions in the potential surface, possibly reaching the threshold size needed for  
472 catastrophic drainage to occur. This would seem likely to mobilise large quantities of sediment,  
473 leading to possible esker formation in a transient subglacial drainage system. Such a mechanism  
474 could help explain the occurrence, size, and also the rarity, of modern mid-latitude Martian  
475 eskers.

## 476 **5 Conclusions**

477 Our results show that the HRA reported by *Orosei et al.*, [2108] beneath the Martian  
478 SPLD does not occupy a depression in the subglacial hydraulic potential surface as calculated  
479 using subglacial hydraulic theory and the surface and basal topographies. This finding is robust  
480 to random perturbations of the bed DEM using the mean and standard deviation of elevation  
481 difference (calculated from the set of points within the Fresnel radius for each point), to different  
482 interpolation resolutions, and to different assumed densities for the inferred liquid layer. For the  
483 latter case, a higher assumed density increases the effect of the bed topography on the subglacial  
484 potential surface, as expected from subglacial hydraulic potential theory (Eq. 2, *Shreve*, [1972]),  
485 and makes predicted lake locations both larger in extent, and more numerous. Three substantial  
486 depressions in the potential surface, with areas between one-third and three-quarters of the area  
487 of HRA, are predicted to occur within  $\sim$ 20 km of the HRA, and a major drainage axis in the  
488 potential surface crosses the HRA in over 90% of the perturbed topographies, a topography  
489 calculated using the mean in-radius elevation, and a topography calculated from the mean  
490 elevation of the set of 1000 perturbed topographies. The areas occupied by these depressions do

491 not show high radar reflectance in the MARSIS data, and therefore show no sign of liquid water  
492 [*Orosei et al. 2018*].

493 The methodology we develop here to acknowledge the uncertainty in radar-derived bed  
494 elevation data adds confidence to our findings. Flow accumulation calculations require the  
495 gradient in the bed elevation to be calculated, and as such are very sensitive to noise in the point-  
496 cloud data used to produce interpolated DEMs. Assessing the local variation in the inferred  
497 topography using the inherent spatial overlap between the individual sensor measurements  
498 (given the large footprint on the MARSIS instrument relative to the measurement frequency)  
499 allows us to calculate the statistical properties of the bed elevation estimates around each original  
500 point, and hence of the uncertainties in the estimated bed elevation. These statistics then allow  
501 realistic random noise values to be added to the point-cloud data in a form of Monte-Carlo  
502 analysis, which allows the calculation of both the mean elevation of pixels in the individual  
503 perturbed topographies, and the mean values from any analysis using the individual perturbed  
504 topographies. For analyses that require the gradient of the topography to be calculated, this  
505 procedure adds valuable robustness to the calculated values.

506 We suggest that if the HRA is due to the presence of liquid water, or at least water-  
507 saturated basal sediments, the location of the HRA seems likely to be due to locally-forced in-  
508 situ basal melting, rather than the melt occurring elsewhere and the resulting liquid then  
509 collecting in an area of low hydraulic potential as is typical for terrestrial subglacial lakes. This  
510 supports the argument made by *Sori and Bramson* [2019] that localized geothermal heating is the  
511 heat source required for melt to occur. Given that the subglacial potential surface in the HRA  
512 does not show any substantial depressions, but instead seems to include a major predicted  
513 drainage axis, the area of inferred basal melt seems to be pinned in-situ, presumably by the  
514 surrounding cold-based ice which acts as an effective aquiclude and prevents movement of the  
515 liquid down the subglacial potential surface. We suggest that the HRA does not represent a ‘true’  
516 subglacial lake, pinned by topography, but that if it does represent liquid water, it is more likely  
517 to be a brine-enriched sludge, or to consist of shallow (but spatially extensive) brine pools as  
518 suggested by *Orosei et al.* [2018].

519

## 520 **Acknowledgments**

521 The MARSIS instrument and experiment were funded by the Italian Space Agency and  
522 NASA. It was developed by the University of Rome, Italy, in partnership with NASA's Jet  
523 Propulsion Laboratory [JPL], Pasadena, CA. The Mars Express and Mars Global Surveyor  
524 missions are operated by the space agencies of the United States (NASA), Europe (European  
525 Space Agency) and Italy (Agenzia Spaziale Italiana). We particularly thank Roberto Orosei for  
526 providing the raw MARSIS data, including the inferred elevation of the basal reflector, used in  
527 *Orosei et al.*, [2018]. Parts of this work were undertaken whilst FEGB was in receipt of a UK  
528 STFC funded PhD studentship, grant number ST/N50421X/1. The authors declare no competing  
529 interests. Code and derived data developed during this research are available at:  
530 <https://doi.org/10.17863/CAM.41622>. MARSIS data used in this study are available in the  
531 repository maintained by *Orosei et al.* [2018] at <http://doi.org/10.5281/zenodo.1285179>. MOLA  
532 data are available from the PDS Geosciences node at: [http://pds-  
533 geosciences.wustl.edu/missions/mgs/megdr.html](http://pds-geosciences.wustl.edu/missions/mgs/megdr.html).

535 **References**

- 536 Arfstrom, J., & Hartmann, W. K. (2005). Martian flow features, moraine-like ridges, and gullies:  
 537 Terrestrial analogs and interrelationships. *Icarus*, *174*(2), 321–335.  
 538 <https://doi.org/10.1016/j.icarus.2004.05.026>
- 539 Arnold, N. (2010). A new approach for dealing with depressions in digital elevation models  
 540 when calculating flow accumulation values. *Progress in Physical Geography: Earth and*  
 541 *Environment*, *34*(6), 781–809. <https://doi.org/10.1177/0309133310384542>
- 542 Baker, D. M. H., & Head, J. W. (2015). Extensive Middle Amazonian mantling of debris aprons  
 543 and plains in Deuteronilus Mensae, Mars: Implications for the record of mid-latitude  
 544 glaciation. *Icarus*, *260*, 269–288. <https://doi.org/10.1016/j.icarus.2015.06.036>
- 545 Bernhardt, H., Hiesinger, H., Reiss, D., Ivanov, M., & Erkeling, G. (2013). Putative eskers and  
 546 new insights into glacio-fluvial depositional settings in southern Argyre Planitia, Mars.  
 547 *Planetary and Space Science*, *85*, 261–278. <https://doi.org/10.1016/j.pss.2013.06.022>
- 548 Björnsson, H., & Guðmundsson, M. T. (1993). Variations in the thermal output of the subglacial  
 549 Grímsvötn Caldera, Iceland. *Geophysical Research Letters*, *20*(19), 2127–2130.  
 550 <https://doi.org/10.1029/93GL01887>
- 551 Bramson, A. M., Byrne, S., & Bapst, J. (2017). Preservation of Midlatitude Ice Sheets on Mars:  
 552 Mars Midlatitude Ice Sheet Preservation. *Journal of Geophysical Research: Planets*,  
 553 *122*(11), 2250–2266. <https://doi.org/10.1002/2017JE005357>
- 554 Butcher, F. E. G., Conway, S. J., & Arnold, N. S. (2016). Are the Dorsa Argentea on Mars  
 555 eskers? *Icarus*, *275*, 65–84. <https://doi.org/10.1016/j.icarus.2016.03.028>
- 556 Butcher, F. E. G., Balme, M. R., Gallagher, C., Arnold, N. S., Conway, S. J., Hagermann, A., &  
 557 Lewis, S. R. (2017). Recent basal melting of a mid-latitude glacier on Mars. *Journal of*  
 558 *Geophysical Research: Planets*, *122*(12), 2445–2468.  
 559 <https://doi.org/10.1002/2017JE005434>
- 560 Clark, C. D., Ely, J. C., Greenwood, S. L., Hughes, A. L. C., Meehan, R., Barr, I. D., et al.  
 561 (2018). BRITICE Glacial Map, version 2: a map and GIS database of glacial landforms  
 562 of the last British-Irish Ice Sheet. *Boreas*, *47*(1), 11–e8. <https://doi.org/10.1111/bor.12273>
- 563 Conway, S. J., Butcher, F. E. G., de Haas, T., Deijns, A. A. J., Grindrod, P. M., & Davis, J. M.  
 564 (2018). Glacial and gully erosion on Mars: A terrestrial perspective. *Geomorphology*,  
 565 *318*, 26–57. <https://doi.org/10.1016/j.geomorph.2018.05.019>
- 566 Evatt, G. W., & Fowler, A. C. (2007). Cauldron subsidence and subglacial floods. *Annals of*  
 567 *Glaciology*, *45*, 163–168. <https://doi.org/10.3189/172756407782282561>
- 568 Fassett, C. I., Dickson, J. L., Head, J. W., Levy, J. S., & Marchant, D. R. (2010). Supraglacial  
 569 and proglacial valleys on Amazonian Mars. *Icarus*, *208*(1), 86–100.  
 570 <https://doi.org/10.1016/j.icarus.2010.02.021>
- 571 Fastook, J. L., Head, J. W., Marchant, D. R., & Forget, F. (2008). Tropical mountain glaciers on  
 572 Mars: Altitude-dependence of ice accumulation, accumulation conditions, formation  
 573 times, glacier dynamics, and implications for planetary spin-axis/orbital history. *Icarus*,  
 574 *198*(2), 305–317. <https://doi.org/10.1016/j.icarus.2008.08.008>
- 575 Fastook, J. L., Head, J. W., Marchant, D. R., Forget, F., & Madeleine, J.-B. (2012). Early Mars  
 576 climate near the Noachian–Hesperian boundary: Independent evidence for cold  
 577 conditions from basal melting of the south polar ice sheet (Dorsa Argentea Formation)  
 578 and implications for valley network formation. *Icarus*, *219*(1), 25–40.

579 <https://doi.org/10.1016/j.icarus.2012.02.013>

580 Fisher, D. A., Hecht, M. H., Kounaves, S. P., & Catling, D. C. (2010). A perchlorate brine  
581 lubricated deformable bed facilitating flow of the north polar cap of Mars: Possible  
582 mechanism for water table recharging. *Journal of Geophysical Research*, *115*, E00E12,  
583 <https://doi.org/10.1029/2009JE003405>

584 Flowers, G. E. (2015). Modelling water flow under glaciers and ice sheets. *Proceedings of the*  
585 *Royal Society A: Mathematical, Physical and Engineering Sciences*, *471*(2176),  
586 20140907–20140907. <https://doi.org/10.1098/rspa.2014.0907>

587 Fowler, A. C. (1999). Breaking the seal at Grímsvötn, Iceland. *Journal of Glaciology*, *45*(151),  
588 506–516. <https://doi.org/10.1017/S0022143000001362>

589 Fricker, H. A., & Scambos, T. (2009). Connected subglacial lake activity on lower Mercer and  
590 Whillans Ice Streams, West Antarctica, 2003–2008. *Journal of Glaciology*, *55*(190),  
591 303–315. <https://doi.org/10.3189/002214309788608813>

592 Fricker, H. A., Scambos, T., Bindschadler, R., & Padman, L. (2007). An active subglacial water  
593 system in West Antarctica mapped from space. *Science*, *315*(5818), 1544–1548.  
594 <https://doi.org/10.1126/science.1136897>

595 Gallagher, C., & Balme, M. (2015). Eskers in a complete, wet-based glacial system in the  
596 Phlegra Montes region, Mars. *Earth and Planetary Science Letters*, *431*, 96–109.  
597 <https://doi.org/10.1016/j.epsl.2015.09.023>

598 Head, J. W., Mustard, J. F., Kreslavsky, M. A., Milliken, R. E., & Marchant, D. R. (2003).  
599 Recent ice ages on Mars. *Nature*, *426*(6968), 797–802.  
600 <https://doi.org/10.1038/nature02114>

601 Kress, A. M., & Head, J. W. (2015). Late Noachian and early Hesperian ridge systems in the  
602 south circumpolar Dorsa Argentea Formation, Mars: Evidence for two stages of melting  
603 of an extensive late Noachian ice sheet. *Planetary and Space Science*, *109–110*, 1–20.  
604 <https://doi.org/10.1016/j.pss.2014.11.025>

605 Le Brocq, A. M., Payne, A. J., Siegert, M. J., & Alley, R. B. (2009). A subglacial water-flow  
606 model for West Antarctica. *Journal of Glaciology*, *55*(193), 879–888.  
607 <https://doi.org/10.3189/002214309790152564>

608 Levy, J. S., Fassett, C. I., Head, J. W., Schwartz, C., & Watters, J. L. (2014). Sequestered glacial  
609 ice contribution to the global Martian water budget: Geometric constraints on the volume  
610 of remnant, midlatitude debris-covered glaciers. *Journal of Geophysical Research:*  
611 *Planets*, *119*(10), 2188–2196. <https://doi.org/10.1002/2014JE004685>

612 Levy, J. S., Fassett, C. I., & Head, J. W. (2016). Enhanced erosion rates on Mars during  
613 Amazonian glaciation. *Icarus*, *264*, 213–219. <https://doi.org/10.1016/j.icarus.2015.09.037>

614 Livingstone, S. J., Clark, C. D., & Tarasov, L. (2013a). Modelling North American palaeo-  
615 subglacial lakes and their meltwater drainage pathways. *Earth and Planetary Science*  
616 *Letters*, *375*, 13–33. <https://doi.org/10.1016/j.epsl.2013.04.017>

617 Livingstone, S. J., Clark, C. D., Woodward, J., & Kingslake, J. (2013b). Potential subglacial lake  
618 locations and meltwater drainage pathways beneath the Antarctic and Greenland ice  
619 sheets. *The Cryosphere*, *7*(6), 1721–1740. <https://doi.org/10.5194/tc-7-1721-2013>

620 Llubes, M., Lanseau, C., & Rémy, F. (2006). Relations between basal condition, subglacial  
621 hydrological networks and geothermal flux in Antarctica. *Earth and Planetary Science*  
622 *Letters*, *241*(3–4), 655–662. <https://doi.org/10.1016/j.epsl.2005.10.040>

623 Martos, Y. M., Catalán, M., Jordan, T. A., Golynsky, A., Golynsky, D., Eagles, G., & Vaughan,  
624 D. G. (2017). Heat Flux Distribution of Antarctica Unveiled. *Geophysical Research*



625 *Letters*, 44(22), 11,417–11,426. <https://doi.org/10.1002/2017GL075609>

626 Nye, J. F. (1976). Water flow in glaciers: jökulhlaups, tunnels and veins. *Journal of Glaciology*,  
627 17(76), 181–207. <https://doi.org/10.1017/S002214300001354X>

628 Orosei, R., Lauro, S. E., Pettinelli, E., Cicchetti, A., Coradini, M., Cosciotti, B., et al. (2018).  
629 Radar evidence of subglacial liquid water on Mars. *Science*, eaar7268.  
630 <https://doi.org/10.1126/science.aar7268>

631 Pattyn, F. (2010). Antarctic subglacial conditions inferred from a hybrid ice sheet/ice stream  
632 model. *Earth and Planetary Science Letters*, 295(3–4), 451–461.  
633 <https://doi.org/10.1016/j.epsl.2010.04.025>

634 Plaut, J. J., Picardi, G., Safaeinili, A., Ivanov, A. B., Milkovich, S. M., Cicchetti, A., et al.  
635 (2007). Subsurface radar sounding of the south polar layered deposits of Mars. *Science*,  
636 316(5821), 92–95. <https://doi.org/10.1126/science.1139672>

637 Scanlon, K. E., Head, J. W., Fastook, J. L., & Wordsworth, R. D. (2018). The Dorsa Argentea  
638 Formation and the Noachian-Hesperian climate transition. *Icarus*, 299, 339–363.  
639 <https://doi.org/10.1016/j.icarus.2017.07.031>

640 Shreve, R. L. (1972). Movement of water in glaciers. *Journal of Glaciology*, 11(62), 205–214.  
641 <https://doi.org/10.1017/S002214300002219X>

642 Shreve, R.L., 1985. Late Wisconsin ice-surface profile calculated from Esker paths and types.  
643 Katahdin Esker System, Maine. *Quaternary Research* 23, 27–37.  
644 [https://doi.org/10.1016/0033-5894\(85\)90069-9](https://doi.org/10.1016/0033-5894(85)90069-9).

645 Smith, D. E., Zuber, M. T., Frey, H. V., Garvin, J. B., Head, J. W., Muhleman, D. O., et al.  
646 (2001). Mars Orbiter Laser Altimeter: Experiment summary after the first year of global  
647 mapping of Mars. *Journal of Geophysical Research: Planets*, 106(E10), 23689–23722.  
648 <https://doi.org/10.1029/2000JE001364>

649 Sori, M. M., & Bramson, A. M. (2019). Water on Mars, with a grain of salt: local heat anomalies  
650 are required for basal melting of ice at the south pole today. *Geophysical Research*  
651 *Letters*, 46(3), 1222–1231. <https://doi.org/10.1029/2018GL080985>

652 Souness, C., & Hubbard, B. (2012). Mid-latitude glaciation on Mars. *Progress in Physical*  
653 *Geography: Earth and Environment*, 36(2), 238–261.  
654 <https://doi.org/10.1177/0309133312436570>

655 Spring, U., & Hutter, K. (1981). Numerical studies of Jökulhlaups. *Cold Regions Science and*  
656 *Technology*, 4(3), 227–244. [https://doi.org/10.1016/0165-232X\(81\)90006-9](https://doi.org/10.1016/0165-232X(81)90006-9)

657 Storrar, R. D., Stokes, C. R., & Evans, D. J. A. (2013). A map of large Canadian eskers from  
658 Landsat satellite imagery. *Journal of Maps*, 9(3), 456–473.  
659 <https://doi.org/10.1080/17445647.2013.815591>

660 Stroeven, A. P., Hättestrand, C., Kleman, J., Heyman, J., Fabel, D., Fredin, O., et al. (2016).  
661 Deglaciation of Fennoscandia. *Quaternary Science Reviews*, 147, 91–121.  
662 <https://doi.org/10.1016/j.quascirev.2015.09.016>

663 Tanaka, K.L., Skinner, J.A., Jr., Dohm, J.M., Irwin, R.P., III, Kolb, E.J., Fortezzo, C.M., Platz,  
664 T., Michael, G.G., and Hare, T.M., (2014), Geologic map of Mars:  
665 U.S. Geological Survey Scientific Investigations Map 3292, scale 1:20,000,000,  
666 pamphlet 43 p., <http://dx.doi.org/10.3133/sim3292>

667 Wieczorek, M. (2008). Constraints on the composition of the Martian south polar cap from  
668 gravity and topography. *Icarus*, 196(2), 506–517.  
669 <https://doi.org/10.1016/j.icarus.2007.10.026>

670 Willis, I. C., Pope, E. L., Leysinger Vieli, G. J.-M. C., Arnold, N. S., & Long, S. (2016).

671 Drainage networks, lakes and water fluxes beneath the Antarctic ice sheet. *Annals of*  
672 *Glaciology*, 57(72), 96–108. <https://doi.org/10.1017/aog.2016.15>  
673 Wingham, D. J., Siegert, M. J., Shepherd, A., & Muir, A. S. (2006). Rapid discharge connects  
674 Antarctic subglacial lakes. *Nature*, 440(7087), 1033–1036.  
675 <https://doi.org/10.1038/nature04660>  
676 Wordsworth, R., Forget, F., Millour, E., Head, J. W., Madeleine, J.-B., & Charnay, B. (2013).  
677 Global modelling of the early Martian climate under a denser CO<sub>2</sub> atmosphere: Water  
678 cycle and ice evolution. *Icarus*, 222(1), 1–19.  
679 <https://doi.org/10.1016/j.icarus.2012.09.036>  
680 Wright, A. P., Siegert, M. J., Le Brocq, A. M., & Gore, D. B. (2008). High sensitivity of  
681 subglacial hydrological pathways in Antarctica to small ice-sheet changes. *Geophysical*  
682 *Research Letters*, 35(17). <https://doi.org/10.1029/2008GL034937>  
683 Zuber, M. T., Phillips, R. J., Andrews-Hanna, J. C., Asmar, S. W., Konopliv, A. S., Lemoine, F.  
684 G., et al. (2007). Density of Mars' south polar layered deposits. *Science*, 317(5845),  
685 1718–1719. <https://doi.org/10.1126/science.1146995>  
686  
687

688 **Figure Captions**

689 **Figure 1. a.** Map of the SPLD, showing the region containing the HRA argued to be subglacial  
690 liquid by *Orosei et al.*, [2018]. The surface topography is taken from the MOLA topographic  
691 dataset [*Smith et al.*, 2001]. The black contour shows the outline of the late Amazonian polar cap  
692 (lApc) unit [*Tanaka et al.*, 2014]; the black square delineates the area investigated in *Orosei et*  
693 *al.*, [2018], and which we investigate in this study. **b.** MOLA surface topography of the study  
694 area highlighted by the black square in a. The red contour shows the location of the HRA  
695 reported by *Orosei et al.*, [2018]. Color scale for both maps shows MOLA elevation in m; X and  
696 Y axes in B are distances in km from the center of the study area.

697 **Figure 2.** MARSIS points for the  $200 \times 200$  km area containing the HRA (red contour) reported  
698 by *Orosei et al.*, [2018], shown in Figure 1. **a.** Unadjusted (raw) bed elevation (m). **b-d.** Mean  
699 (**b**), median (**c**) and standard deviation (**d**) of elevation difference (m) between each point and the  
700 set of points within the sensor Fresnel radius. X and Y axis units are km from the center of the  
701 area; color scale units are meters. Dots are scaled to the Fresnel radius of  $\sim 4$  km.

702 **Figure 3.** Frequency distributions of the elevation differences for each point and its neighbours  
703 within the Fresnel radius for that point. **a.** Overall distribution for all points. **b.** The point with  
704 the maximum mean elevation difference. **c.** The point with the minimum mean elevation  
705 difference. **d.** The point with the maximum standard deviation of elevation difference. X axis  
706 units are meters of elevation difference; Y axis units are point counts. Red line shows the best-fit  
707 normal distribution.

708 **Figure 4.** Gridded 200 m topography of study area sub-ice bed based on: **a.** raw MARSIS radar  
709 data (Figure 2a, *Orosei et al.*, [2018]; **b-c:** mean (**b**) and median (**c**) elevation of all points in the  
710 Fresnel radius of each original point (Figure 2b-c); **d.** mean elevation of the 1000 perturbed  
711 topographies (see text). X and Y axis units are km from the center of the area; color scale shows  
712 elevation in meters. The red contour shows the HRA reported by *Orosei et al.*, [2018].

713 **Figure 5.** Calculated flow accumulation values at 200 m resolution for: **a.** Interpolated raw  
714 topography. **b.** Mean in-radius topography. **c.** Median in-radius topography. **d.** Mean-perturbed  
715 topography (see text). X and Y axis units are km from the center of the area; color scale units are  
716 the common logarithm of the upstream area flowing into each cell in  $\text{km}^2$ . The red contour shows  
717 the HRA reported by *Orosei et al.*, [2018].

718 **Figure 6.** Calculated flow accumulation grids at 200 m resolution for the central region around  
719 the HRA: **a.** Interpolated raw topography. **b.** Mean in-radius topography. **c.** Median in-radius  
720 topography. **d.** Mean-perturbed topography (see text). X and Y axis units are km from the center  
721 of the area; color scale units are the common logarithm of the upstream area flowing into each  
722 cell in  $\text{km}^2$ . The red contour shows the HRA reported by *Orosei et al.*, [2018].

723 **Figure 7. a-b.** Results of the 1000 perturbed-topography experiments at 200 m resolution **a.**  
724 Probability value that any given DEM cell is within a lake for the set of 1000 perturbed-  
725 topography runs. **b.** Mean upstream area for the flow accumulation algorithm results. **c-f.** Results  
726 of the variable liquid and ice density experiments using the 200 m mean-perturbed topography  
727 (shown in Figure 4d). **c.** Probability value that any given DEM cell is within a lake for the

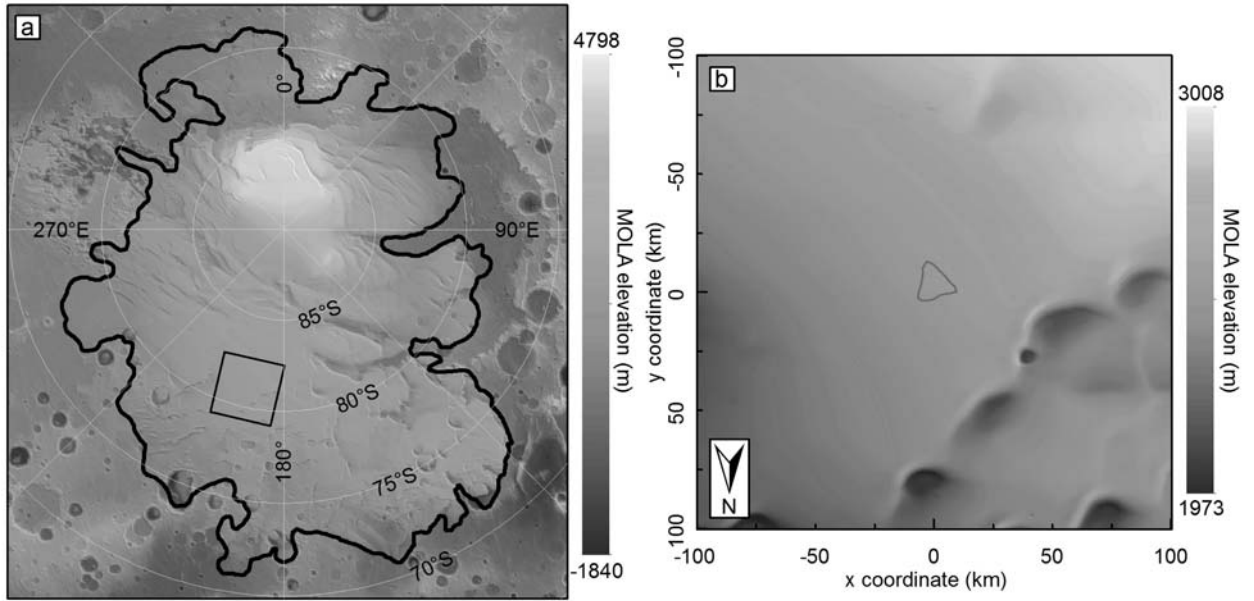
728 variable liquid density experiments. **d.** Mean upstream area for the flow accumulation algorithm  
729 runs. **e.** Calculated flow accumulation grid for the  $\rho_w = 1000 \text{ kg m}^{-3}$  experiment with standard  $\rho_i$ .  
730 **f.** Calculated flow accumulation grid for the  $\rho_i = 1200 \text{ kg m}^{-3}$ ,  $\rho_w = 1000 \text{ kg m}^{-3}$  experiment.  
731 Color scale units for a and c are probability values;  $P = 0$  shows a pixel was never calculated to  
732 be in a lake;  $P = 1$  shows a pixel was calculated to be in a lake in all simulations. Color scale  
733 units for b, d, e and f are the common logarithm of the upstream area flowing into each cell in  
734  $\text{km}^2$ . X and Y axis units are km from the center of the area. The red contour shows the HRA  
735 reported by *Orosei et al.*, [2018]. Black line labeled X–Y in Panel B shows the location of the  
736 transect shown in Figure 9.

737 **Figure 8.** Mean upstream area for the set of 1000 reduced resolution perturbed topography runs.  
738 **a.** 500 m resolution. **b.** 1000 m resolution. **c.** 2500 m resolution. **d.** 5000 m resolution. Color  
739 scale units are the common logarithm of the upstream area flowing into each cell in  $\text{km}^2$ . X and  
740 Y axis units are km from the center of the area. The red contour shows the HRA reported by  
741 *Orosei et al.*, [2018].

742 **Figure 9.** Cross-section through the HRA along transect X–Y shown in Figure 7b. Basal  
743 topography is from the 200 m mean-perturbed DEM. The black arrow shows the extent of the  
744 HRA. Note the discontinuity in the left-hand Yaxis to improve visibility of the basal topography.

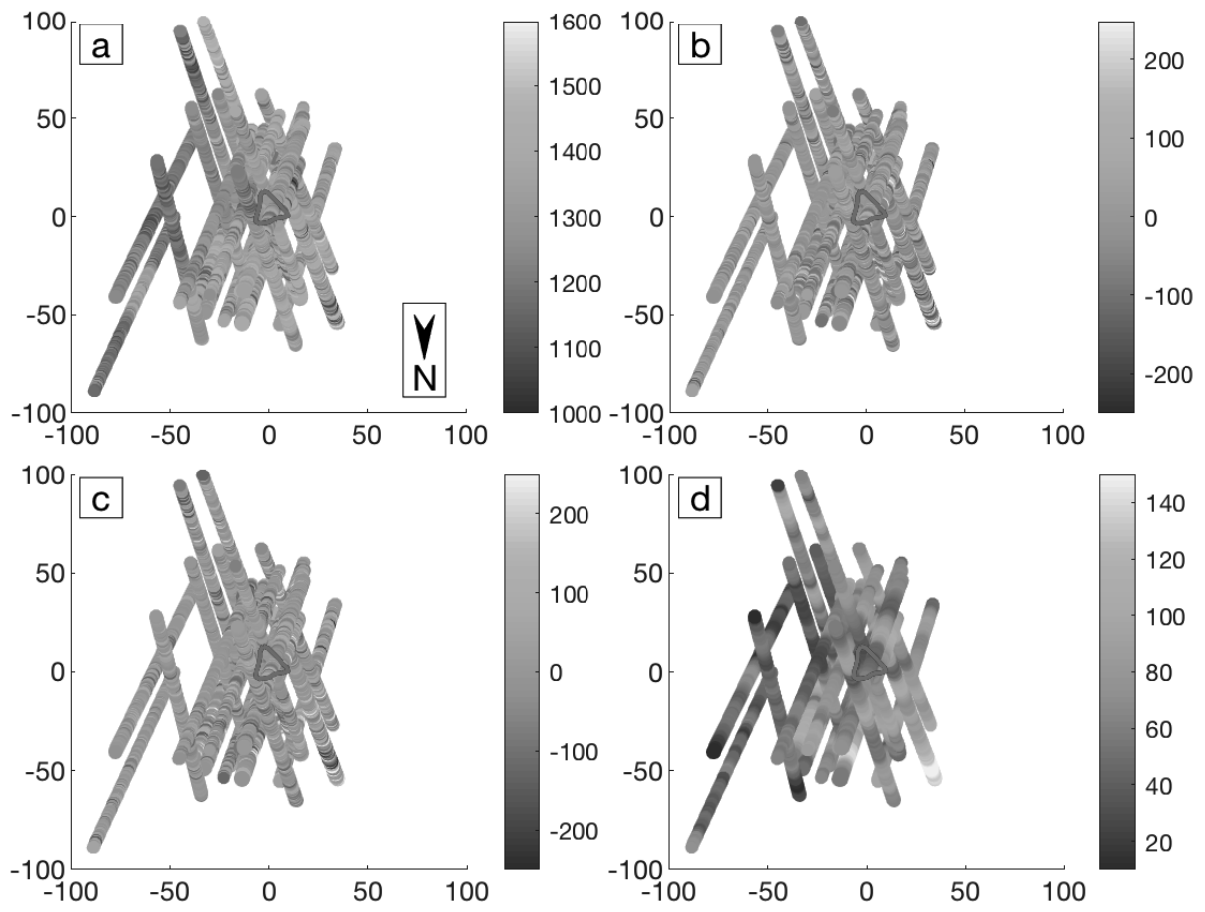
745  
746

747 Figure 1:



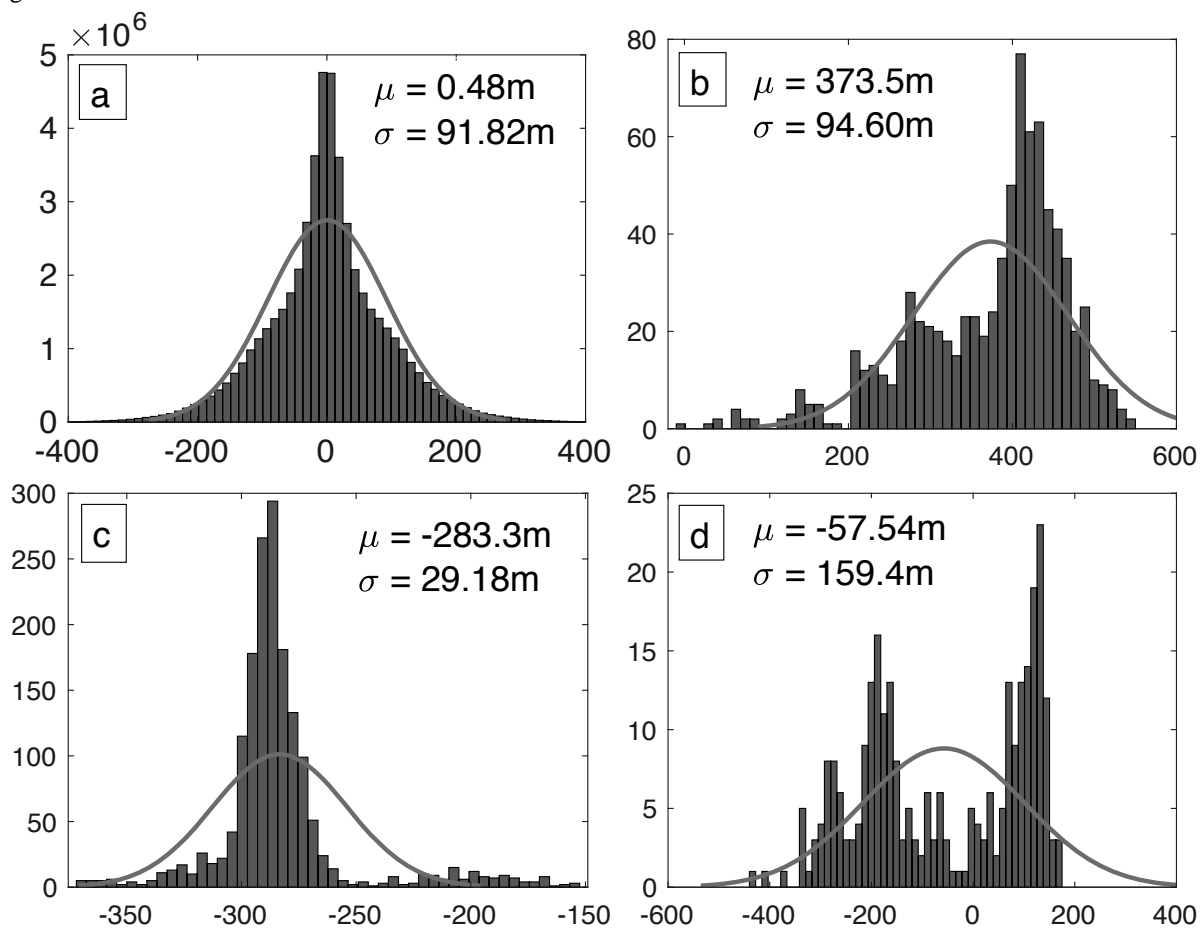
748  
749

750 Figure 2



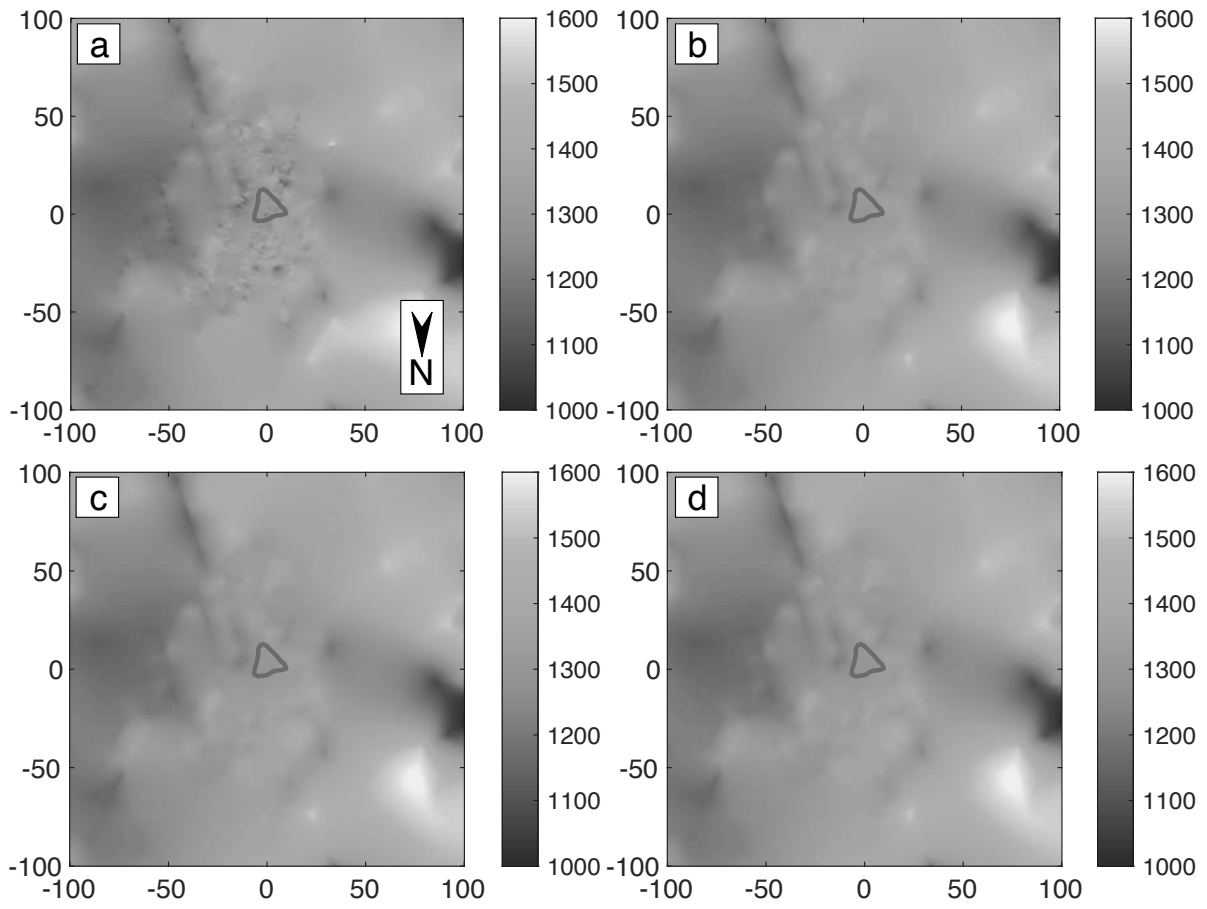
751  
752  
753

754 Figure 3



755  
756  
757

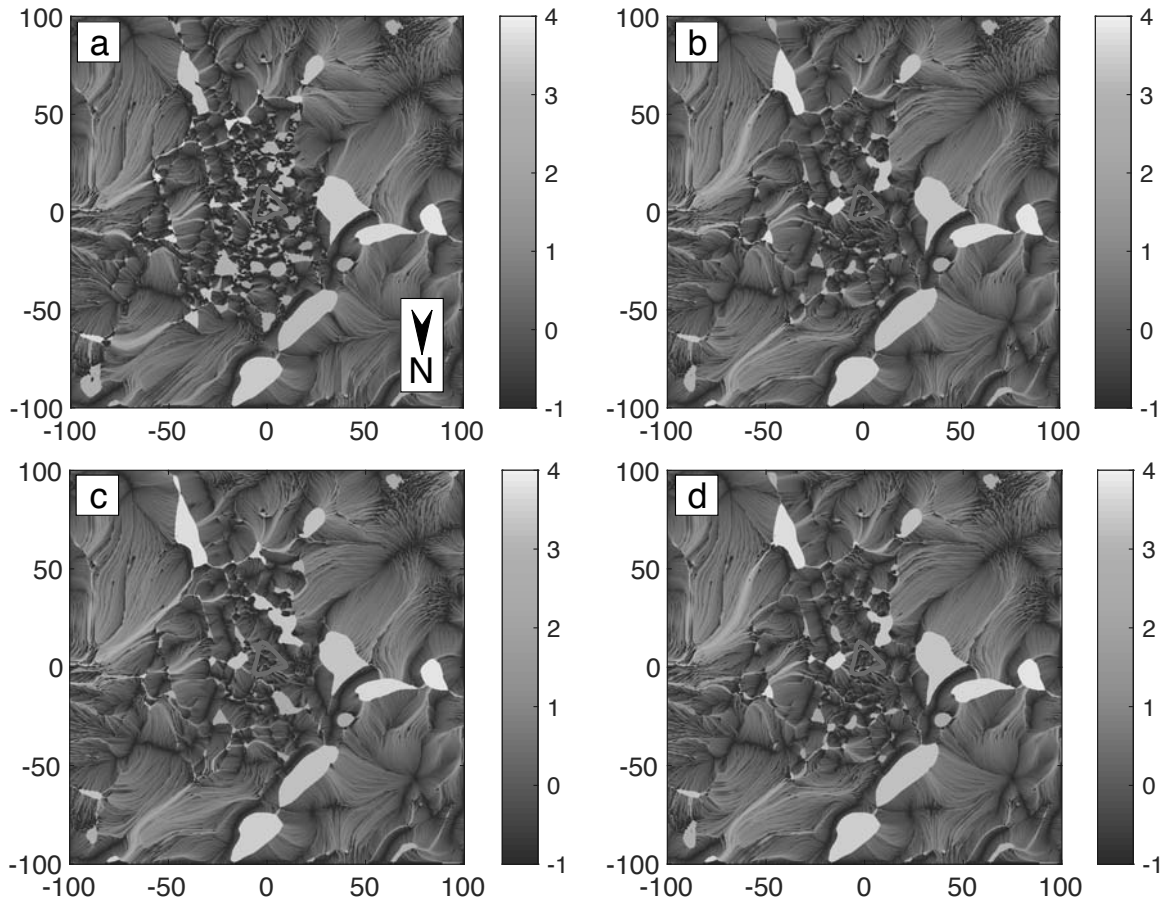
758 Figure 4



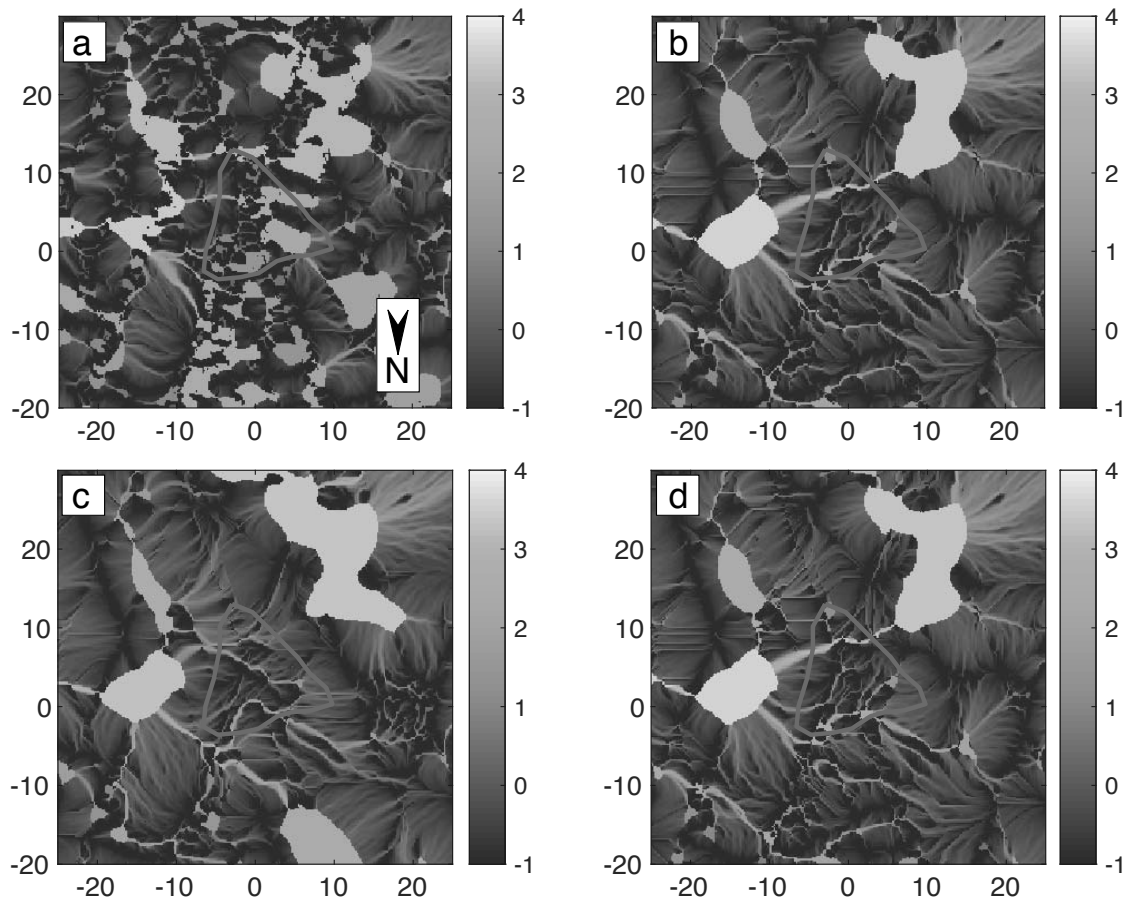
759  
760  
761

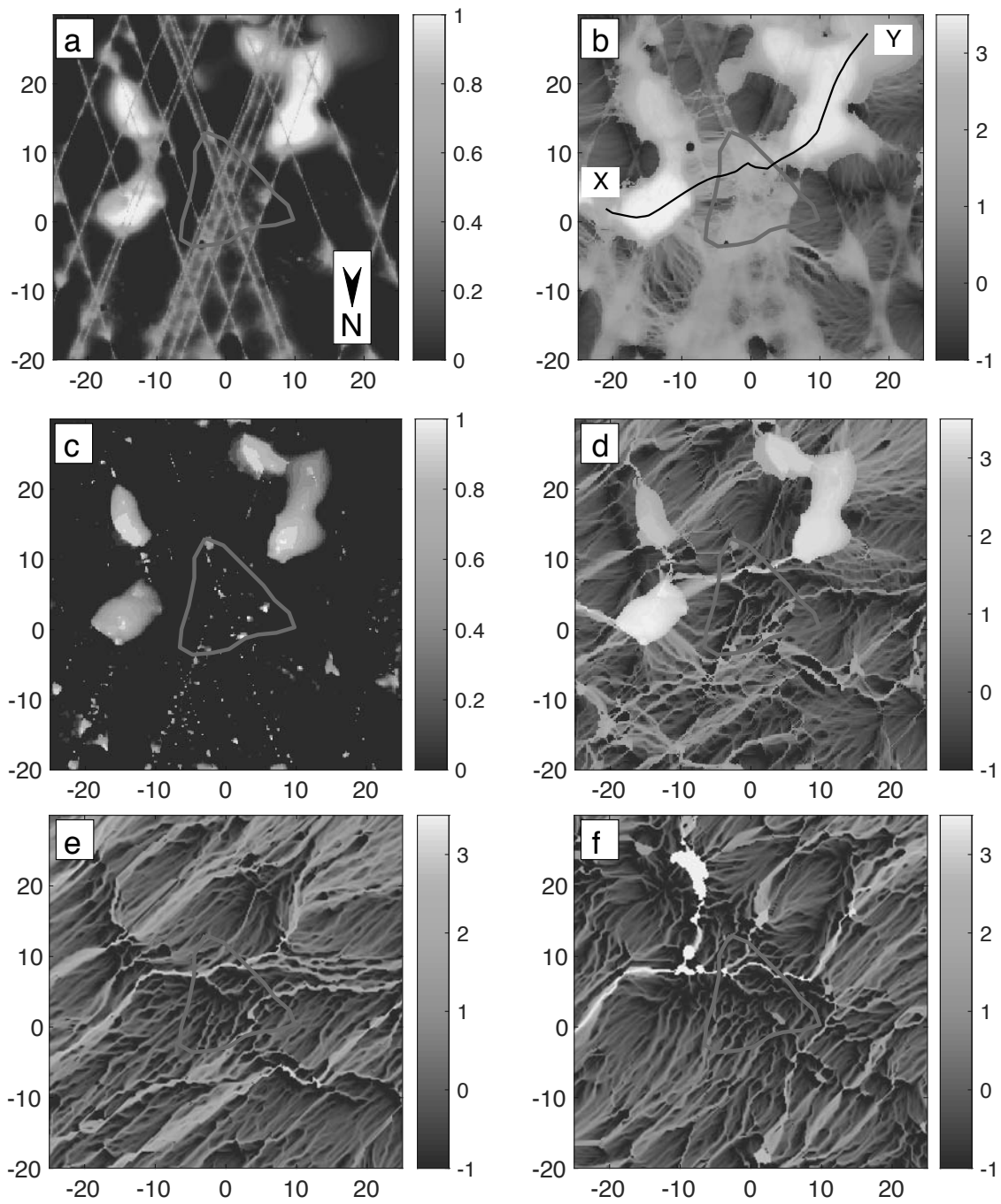


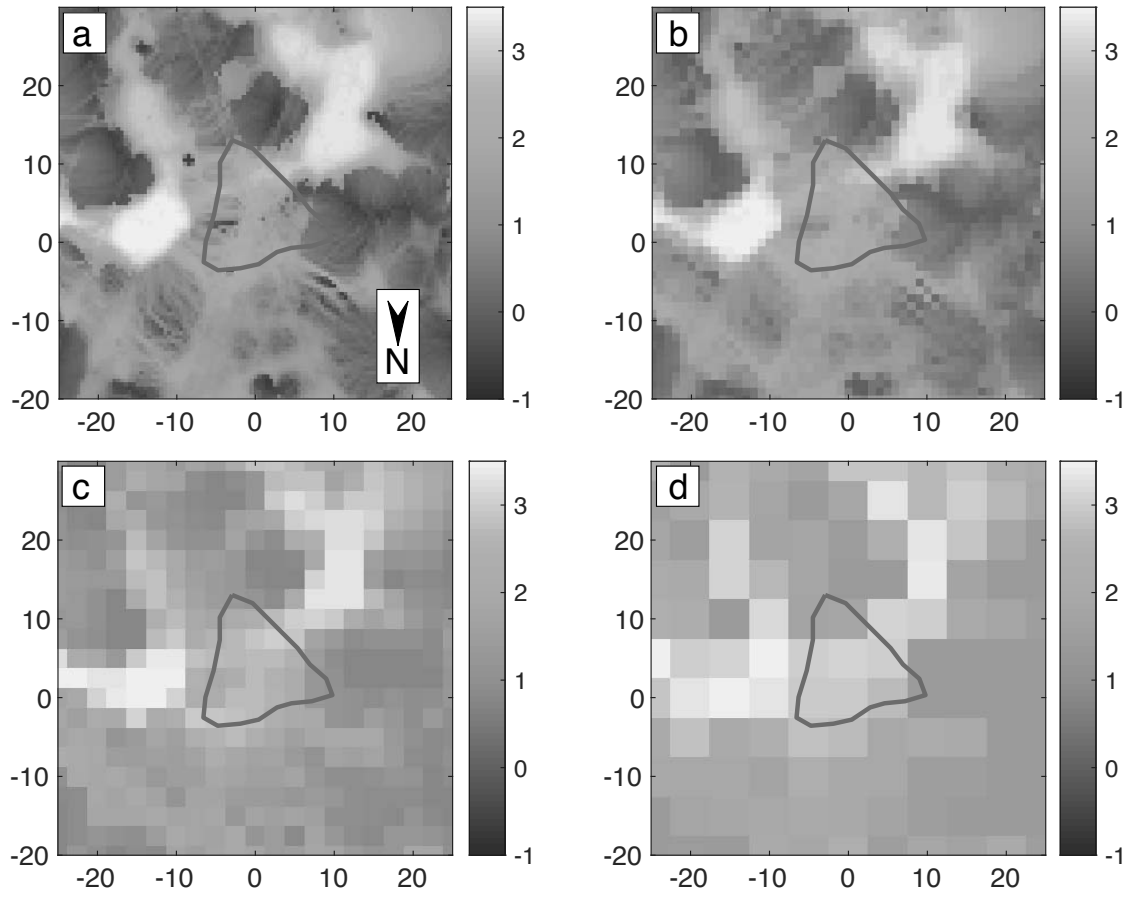
762 Figure 5



763  
764  
765







775  
776  
777

778 Figure 9.

